Proceedings of the 6th International Conference on Computing and Data Science
DOI: 10.54254/2755-2721/86/20241600

A method based on GA solver for optimizing the design parameters of the right frustum resistance frame for indoor earthquake shelters

Xuanyu Cao

Department of Mechanical Engineering and Mechanics, Xiangtan University, Xuelin Road, Yuhu District, Xiangtan, Hunan, China

202321642715@smail.xtu.edu.cn

Abstract. This paper proposes a new method to enhance the impact resistance of earthquake shelters. Traditional methods for protecting individuals during earthquakes focus on improving or reinforcing the building structures, which is time-consuming and inflexible. The SHELTER project developed an earthquake shelter using a conventional cubic frame. This study builds upon the SHELTER project by optimizing its frame structure to improve the shelter's impact resistance against falling debris during an earthquake. Firstly, a right frustum frame is selected as the basic geometric configuration for optimization (with the cuboid being a particular case of the frustum). Six critical design parameters serve as variables for optimization, establishing a mathematical model. Secondly, to maximize the permissible impact loads in both vertical and horizontal directions (F_1 and F_2), a multi-objective optimization using the NSGA-II algorithm is performed on the selected parameters, resulting in a Pareto front. Furthermore, to choose a solution from the Pareto front that meets the needs of this study, the relationship between the forces F_1 and F_2 applied to the shelter frame by falling debris during an earthquake is examined, converting the multi-objective optimization problem into a single-objective optimization problem. Finally, based on the relationship between F_1 and F_2, a single-objective optimization function is established and solved using the Genetic Algorithm (GA) to obtain the optimal parameters. The shelter frame manufactured with these optimal parameters exhibits better overall impact resistance than the cubic frame. This improvement is attributed not only to the geometric properties of the frustum, which results in a lower centre of gravity, but also to the optimization method, which enhances the frame's vertical impact resistance while maintaining good horizontal impact resistance.

Keywords: Earthquake Shelter Optimization, Right frustum frame, NSGA-II & GA algorithm.

1. Introduction

Earthquakes are triggered by the sudden release of energy in the lithosphere[1], generating seismic waves that cause extensive damage to surrounding areas. According to model predictions, as the global population increases, earthquakes, combined with other concurrent disasters, will result in approximately 2.57 million deaths throughout the 21st century due to building collapses and related hazards[2]. To improve survival rates for people within the seismic wave radiation area during an earthquake, the engineering community has conducted extensive research and verification on seismic-

DOI: 10.54254/2755-2721/86/20241600

resistant structural design and the reinforcement of existing structures[3]. Despite improvements in seismic performance in some buildings, long construction periods and low adoption rates characterize the design of seismic-resistant structures and the reinforcement of existing structures. Therefore, an urgent need exists for a more flexible solution in this field.

The SHELTER project provides a novel solution to save lives in conjunction with Earthquake Early Warning Systems (EEWS)[4]. Upon receiving alerts from the EEWS, individuals inside a building can quickly reach a super-strong protective element within the building. This solution improves survival rates by shortening the distance individuals travel to seek refuge. The project primarily discusses the impact resistance of protective elements with rectangular frame structures but does not address the impact resistance of aspects with other geometric configurations. Therefore, it is possible that improving the geometric configuration could further enhance the impact resistance of these elements.

During an earthquake, protective elements primarily face impacts from debris falling from upper floors. Due to the randomness of falling debris and the fact that it often comes with a tilted angle, the protective elements must have both impact resistance and anti-overturning capabilities to withstand vertical and horizontal impact loads. Based on the geometric evolution of the rectangular structure in the SHELTER project and the inherent impact resistance and anti-overturning properties of frustums, the frustum serves as the initial geometric configuration for optimizing protective elements[5]. Compared to the pyramid and prismatic resistance frames, the frustum resistance frame does not require unique materials to reinforce the top and offers better stability.

Let the maximum vertical impact load that the frustum resistance frame withstands be $F_{1,}$ and the maximum horizontal impact load be F_2. The problem is simplified to maximize F_1 and F_2 under given conditions. For the frustum resistance frame, one of the critical parameters to be optimized is the angle α between the lateral edge and the base of the resistance frame. By using the NSGA-II algorithm[6] to optimize α, the Pareto front of F_1 and F_2 concerning α is obtained. Although all solutions on the Pareto front are optimal combinations of F_1 and F_2, increasing one inevitably reduces the other. In practical scenarios, neither F_1 nor F_2 can be too low. Therefore, it is necessary to introduce the relationship between F_1 and F_2 based on common impact situations of the resistance frame, transforming the multi-objective optimization problem into a single-objective optimization problem to determine the optimal design parameters that meet practical requirements.

2. Methodology

2.1. Development of the mathematical model

In the frame, the beams represent the edges of a right frustum, and different geometrical models of a right frustum with varying numbers of lateral edges, as shown in **Figure 1**, illustrate these constructions. Each geometrical model establishes a coordinate system and labels the relevant parameters. This paper only considers the stability of the right frustum under static conditions, assuming that the base of the right frustum is the long side, ensuring that this frame posture does not quickly become unstable when subjected to impact. The number of lateral edges should be greater than 3 to satisfy three-dimensional geometric conditions. However, considering cost and welding process issues, the number of lateral edges should not be too many, so this paper sets the upper limit of the number of lateral edges to 8. To ensure the accuracy of parameter optimization, the optimization process in this paper temporarily does not consider the addition of extra reinforcing beams.

Vertical impact on the frame induces tension, compression, bending, torsion, and other beam stress conditions. At this point, the impact resistance of the beams depends on weld strength, material properties, the angle between the lateral edge and the base of the frame, the length of each edge, the beams' cross-sectional shape, and the beams' cross-sectional area. During horizontal impact, the frame must ensure damage resistance and toppling prevention. Since the issue of structural damage has been considered in the vertical impact problem, to avoid repetitive calculations, the horizontal impact problem mainly focuses on the anti-toppling ability related to the height of the frame's centre of gravity. Also, since the height of the centre of gravity of the right frustum is related to some of the factors mentioned

DOI: 10.54254/2755-2721/86/20241600

in the vertical impact problem, essential items are directly selected from the factors of vertical impact and abstracted as optimizable parameters. A total of six optimizable parameters are abstracted, namely:

α—The angle between the lateral edge and the bottom surface of the resistance frame, measured in rad.

r_1—The distance from the vertex of the resistance frame's top surface to the centre of the top surface, referred to as the top surface equivalent radius, measured in m.

h—The distance from the top surface of the resistance frame to the bottom surface of the resistance frame, referred to as the height of the resistance frame, measured in meters.

c—The distance from the vertex of the resistance frame profile cross-section to its centre, referred to as the section equivalent radius, measured in meters.

t—The thickness of the resistance frame profile, measured in meters.

n—The number of lateral edges of the resistance frame, $n \in \{3,4,5,6,7,8\}$.

In **Figure 1**, F represents the impact load on the frame. Due to the randomness of the impact load F's direction, this paper selects the F that most easily causes the frame to become unstable for discussion. As shown in **Figure 1**, the F most likely to cause instability appears in the u-w plane. Therefore, F is decomposed along the u-axis and w-axis within the u-w plane, resulting in the vertical impact load F_1 and the horizontal impact load F_2 on different frames, as shown in **Figure 1**. During loading, F_1 and F_2 equal the frame's vertical and horizontal internal forces. Therefore, F_1 and F_2 represent the internal forces of the frame during the loading process. The maximum values that F_1 and F_2 can reach are the maximum vertical impact load and maximum horizontal impact load that the frame can withstand. At this point, the resultant force F of F_1 and F_2 is the maximum impact load that the frame can endure, reflecting the comprehensive impact resistance of the frame.

The maximum value of F is related to six optimizable parameters. Since F_1 and F_2 arise from the decomposition of F, they may simultaneously include specific parameters. If back-calculating the optimal parameters for the quasi-stable model that satisfies the material's mechanical properties while ensuring that both F_1 and F_2 meet the strength criteria, the entire derivation process will involve multiple sets of nonlinear equations, making it difficult to derive an ideal objective function.

Therefore, this study proposes a new reverse expression method. First, an expression for the maximum value of F_2 under the condition that the frame does not topple is derived. Then, based on this F_2 expression and the requirement that the frame does not fail, an expression for F_1 is derived. Based on this foundation, objective functions are formulated separately for multi-objective and single-objective optimization.

Based on the parameters labelled in **Figure 1**, first derive the expression for the centre of gravity h_{gq1} of the frame without counterweights[7], as shown in Equation (1).

$$h_{gq1} = \frac{h(b^2+2ab+3a^2)}{4(b^2+ab+a^2)} \tag{1}$$

Here, a represents the top edge length of the frame, and b represents the bottom edge length of the frame. The profile selected is a cold-formed AISI 1045 steel square tube with a density of about 8 g/cm^3, denoted as ρ_1. Considering the frame's low anti-toppling ability without adding counterweights in practical applications, counterweight sand with a density of approximately 6.5 g/cm^3 (denoted as ρ_2) is assumed to fill inside the bottom edge profile. Based on the densities of the two materials, a new formula for the centre of gravity is established, as shown in Equation (2).

$$h_{gq} = \frac{\rho \cdot h_{gq1} \cdot V_1 + 4\rho_2 \cdot n \cdot c \cdot b \cdot (c-t)^2}{\rho_1 \cdot V_1 + \rho_2 \cdot V_2} \tag{2}$$

Here, V_1 is the volume of the space enclosed by the frame, and V_2 is the space inside the bottom edge of the frame used for filling with counterweight sand. Both expressions are shown in Equation (3)[7].

DOI: 10.54254/2755-2721/86/20241600

$$\begin{cases} V_1 = \frac{h \cdot S_b}{3}\left(1 + \frac{b}{a} + \left(\frac{b}{a}\right)^2\right) \\ V_2 = 4nb(c-t)^2 \end{cases} \tag{3}$$

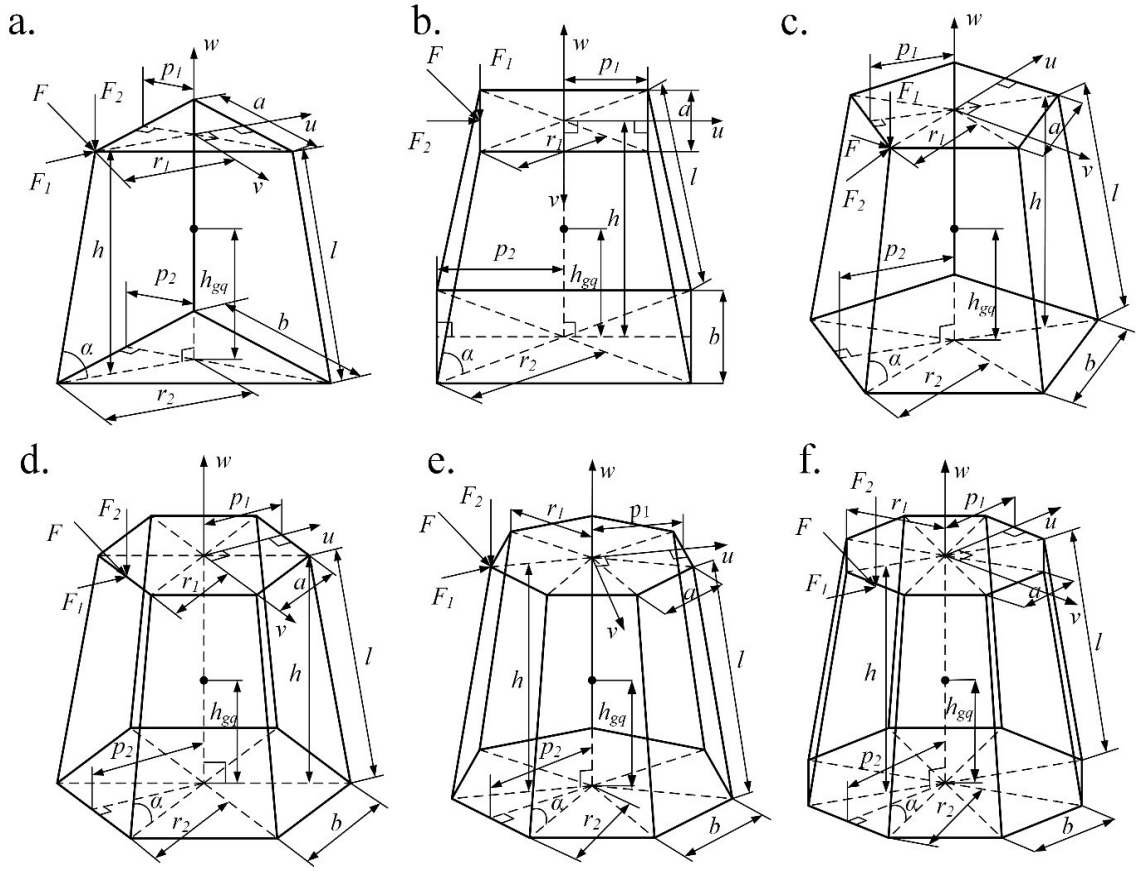

Figure 1. Establishment of coordinate systems and preliminary calibration of optimizable parameters for right frustum resistance frames of different structures. (Note: **a.** Establishment of coordinate systems, loading, and parameters within the frame when *n*=3; **b.** Establishment of coordinate systems, loading, and parameters within the resistance frame when *n*=4; **c.** Establishment of coordinate systems, loading, and parameters within the resistance frame when *n*=5; **d.** Establishment of coordinate systems, loading, and parameters within the resistance frame when *n*=6; **e.** Establishment of coordinate systems, loading, and parameters within the resistance frame when *n*=7; **f.** Establishment of coordinate systems, loading, and parameters within the resistance frame when *n*=8.)

In Equation (3), S_b is the base area of the frame. Equation (4) shows the expression for S_b.

$$S_b = \frac{1}{2} b \cdot n \cdot r_2 \cdot cos\frac{\pi}{n} \tag{4}$$

In Equation (1-4), r_2 is the distance from the corner of the frame's base to the geometric centre of the base. r_2 can be derived from r_1, and the expression for r_2 is shown in Equation (5).

$$r_2 = r_1 + \frac{h}{tan\,\alpha} \tag{5}$$

Since the integral of the horizontal moment concerning the angle equals the work done by the moment, the expression for the work done by gravity G when the resistance frame reaches an unstable state under the action of external force F_2 is shown in Equation (6)[8].

DOI: 10.54254/2755-2721/86/20241600

$$I_G = \int_{\theta_0}^{\frac{\pi}{2}} G \cdot l_{gq} \cdot \cos\theta \, d\theta = G \cdot l_{gq} \left[1 - \sin\left(\arctan\frac{l_{gq}}{p_2}\right)\right] \tag{6}$$

Formula (7) shows the expressions for p_1 and p_2. When the number of lateral edges takes odd or even numbers, the expression for the shortest distance p_{2k} between the projection of the F_2 acting point on the base and the opposite edge of the base is slightly different, as shown in Equation (8).

$$\begin{cases} p_1 = r_1 \cdot \cos\frac{\pi}{n} \\ p_2 = r_2 \cdot \cos\frac{\pi}{n} \end{cases} \tag{7}$$

$$p_{2k} = \begin{cases} r_1 + p_2, n = 2k+1 \\ p_1 + p_2, n = 2(k+1) \end{cases} (k = 1,2,3\ldots) \tag{8}$$

Equation (9) provides the expression for the shortest distance l_{fq} between the action point of F_2 and the opposite edge of the base.

$$l_{fq} = \sqrt{h^2 + p_{2k}^2} \tag{9}$$

Equation (10) expresses the angle γ_0 between l_{fq} and the bottom surface.

$$\gamma_0 = \arctan\frac{h}{p_{2k}} \tag{10}$$

Bringing the resistance frame to an unstable state requires the work I_F by F_2, as expressed in Equation (11).

$$I_F = \int_{\gamma_0}^{\frac{\pi}{2}} F_2 \cdot l_{fq} \cdot \sin\gamma \, d\gamma = F_2 \cdot l_{fq} \cdot \cos\left(\arctan\frac{h}{p_{2k}}\right) \tag{11}$$

Based on the kinetic energy theorem shown in Equation (12)[9], the expression for the required bearing capacity F_{2a} of the resistance frame under the action of external force F_2, taking into account the non-overturning condition, can be derived as shown in Equation (13).

$$I_G = I_F \tag{12}$$

$$F_{2a} = G \cdot l_{gq} \cdot \left[1 - \sin\left(\arctan\frac{h_{gq}}{p_2}\right)\right]\left[l_{fq}\cos\left(\arctan\frac{h}{p_{2k}}\right)\right]^{-1} \tag{13}$$

Hollow steel serves as the initial choice for the resistance frame profile to achieve weight reduction and cost savings. Equation (14) shows the expression for the moment of inertia of a rhombic hollow steel section, while Equation (15) shows the expression for its polar moment of inertia[10].

$$I_z = \iint_A y^2 dA = 4 \cdot \int_0^{\frac{\pi}{2}} \sin^2\theta \, d\theta \int_{\frac{c-\sqrt{2}t}{\sin\theta+\cos\theta}}^{\frac{c}{\sin\theta+\cos\theta}} \rho^3 d\rho = \left[c^4 - (c-\sqrt{2}t)^4\right] \int_0^{\frac{\pi}{2}} \frac{\sin^2\theta}{(\sin\theta+\cos\theta)^4} d\theta \tag{14}$$

$$I_p = \iint_A \rho^2 dA = 4 \cdot \int_0^{\frac{\pi}{2}} d\theta \int_{\frac{c-\sqrt{2}t}{\sin\theta+\cos\theta}}^{\frac{c}{\sin\theta+\cos\theta}} \rho^3 d\rho = \left[c^4 - (c-\sqrt{2}t)^4\right] \int_0^{\frac{\pi}{2}} \frac{1}{(\sin\theta+\cos\theta)^4} d\theta \tag{15}$$

As shown in **Figure 2**, by analysing the spatial force system, the normal stress at the critical point Q_1 on the inner side of the lateral edge in the *u*-*w* plane is the sum of compressive and bending stress. When the normal stress at the critical point is equal to the allowable normal stress $[\sigma]$ ($[\sigma]$=180MPa) of the profile, the expression for the maximum value that F_2 can reach based on this criterion is shown in Equation (16).

$$F_{2b} = [\sigma] \cdot n \cdot s \cdot I_z \left(I_z \cdot \cos\alpha \cdot \cos\frac{\pi}{n} + s \cdot l \cdot c \cdot \sin\frac{\pi}{n}\right)^{-1} \tag{16}$$

DOI: 10.54254/2755-2721/86/20241600

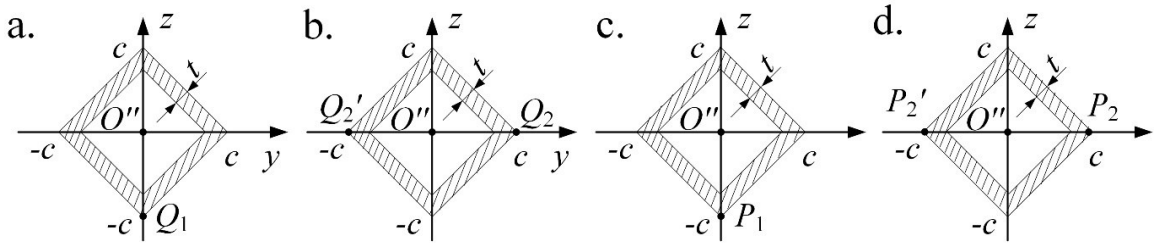

Figure 2. The distribution positions of critical points on the cross-section of the lateral edge. (Note: **a.** The critical point at the bottom of the cross-section related to F_2; **b.** The critical points on both sides of the cross-section related to F_2; **c.** The critical points on both sides of the cross-section related to F_1; **d.** The critical points on both sides of the cross-section related to F_1.)

In Equation (16), s represents the cross-sectional area of the support frame profile, and the expression for s is given in Equation (17).

$$s = 4\sqrt{2}ct - 4t^2 \tag{17}$$

In the u-w plane, the normal stress at the critical points Q_2 and Q_2' on both sides of the lateral edge equals the sum of compressive and bending stress. When the normal stress at the critical points is equal to the allowable normal stress $[\sigma]$ of the profile, the expression for the maximum value that F_2 can reach based on this criterion is shown in Equation (18).

$$F_{2c} = \frac{[\sigma]\cdot n\cdot s\cdot I_z}{I_z\cdot cos\,\alpha\cdot cos\frac{\pi}{n}+s\cdot l\cdot c\cdot sin\,\alpha\cdot cos\frac{\pi}{n}} \tag{18}$$

In the y-z cross-section of the Lateral edge, the shear stress at the critical points Q_2 and Q_2' on both sides of the profile is equal and originates from F_2 and the torque it provides. When the shear stress at these critical points is precisely equal to the allowable shear stress $[\tau]$ ($[\tau]$=90MPa) of the profile, the expression for the maximum value that F_2 can reach based on this criterion is shown in Equation (19).

$$F_{2d} = \frac{2\cdot n\cdot s\cdot I_p[\tau]}{s\cdot a\cdot sin\,\alpha+2\cdot I_p\,sin\frac{\pi}{n}} \tag{19}$$

In the y-z cross-section of the Lateral edge, the shear stress at the critical point Q_1 at the bottom of the profile originates from F_2 and the torque it provides. When the shear stress at this critical point is precisely equal to the allowable shear stress $[\tau]$ of the material, the expression for the maximum value that F_2 can reach based on this criterion is shown in Equation (20).

$$F_{2e} = \frac{2\cdot n\cdot s\cdot I_p[\tau]}{s\cdot a\cdot c\cdot sin\,\alpha+2\cdot I_p\cdot sin\,\alpha\cdot cos\frac{\pi}{n}} \tag{20}$$

Select the smallest F_2 value among the five criteria discussed above, and then assign this processed value to F_2. Equation (21) shows the expression for the new F_2.

$$F_2 = min(F_{2a}, F_{2b}, F_{2c}, F_{2d}, F_{2e}) \tag{21}$$

After determining F_2, the value of F_1 can be subsequently determined based on this. In the y-z cross-section of the Lateral edge, the normal stress at the critical point P_1 at the bottom of the profile comes from the vertical external load F_1 and the horizontal external load F_2 and the bending moment they provide. When the normal stress at this critical point is precisely equal to the allowable normal stress $[\sigma]$ of the profile, the expression for the maximum value that F_1 can reach based on this criterion is shown in Equation (22).

$$F_{1a} = \frac{n\cdot s\cdot I_z\cdot[\sigma]-F_2\cdot\left(I_z\cdot cos\,\alpha\cdot cos\frac{\pi}{n}+s\cdot l\cdot c\cdot sin\frac{\pi}{n}\right)}{I_z\cdot sin\,\alpha+s\cdot l\cdot c\cdot cos\,\alpha} \tag{22}$$

DOI: 10.54254/2755-2721/86/20241600

In the *y-z* cross-section of the Lateral edge, the normal stress at the critical points P_2 and P_2' on both sides of the profile is equal and originates from F_1 and F_2, as well as the bending moment they provide. When the normal stress at these critical points is precisely equal to the allowable normal stress $[\sigma]$ of the profile, the expression for the maximum value that F_1 can reach based on this criterion is shown in Equation (23).

$$F_{1b} = \frac{n \cdot s \cdot I_z \cdot [\sigma] - F_2 \cdot \left(I_z \cdot cos\ \alpha \cdot cos\frac{\pi}{n} + s \cdot l \cdot c \cdot sin\ \alpha \cdot cos\frac{\pi}{n}\right)}{I_z \cdot sin\ \alpha + s \cdot l \cdot c \cdot cos\ \alpha} \tag{23}$$

The shear stress at the critical point P_1 at the bottom of the *y-z* cross-section of the Lateral edge is influenced by F_1 and F_2, as well as the bending moment they provide. When the shear stress at this critical point is precisely equal to the allowable shear stress $[\tau]$ of the profile, the expression for the maximum value that F_1 can reach based on this criterion is shown in Equation (24).

$$F_{1c} = \frac{2n \cdot s \cdot I_z \cdot [\tau] - F_2 \cdot I_p \left(a \cdot sin\ \alpha - 2\ sin\ \alpha \cdot cos\frac{\pi}{n}\right)}{2s \cdot p_{1k} \cdot cos\ \alpha \cdot sin\frac{\pi}{n} + 2I_p\ cos\ \alpha} \tag{24}$$

The shear stress at the critical points P_2 and P_2' on both sides of the *y-z* cross-section of the Lateral edge is equal and originates from F_1 and F_2, as well as the bending moment they provide. When the shear stress at these critical points is precisely equal to the allowable shear stress $[\tau]$ of the profile, the expression for the maximum value that F_1 can reach based on this criterion is shown in Equation (25). Here, p_{1k} represents the distance from the load point or edge on the top surface of the resistance frame to the opposite edge. The expression slightly varies depending on whether the number of lateral edges is odd or even, as shown in Equation (26). The smallest F_1 value among the abovementioned criteria is selected and assigned to F_1. Equation (27) shows the expression for the new F_1.

$$F_{1d} = \frac{2n \cdot s \cdot I_z \cdot [\tau] - F_2 \cdot I_p \left(a \cdot sin\ \alpha + 2\ sin\frac{\pi}{n}\right)}{2s \cdot p_{1k} \cdot cos\ \alpha \cdot sin\frac{\pi}{n}} \tag{25}$$

$$p_{1k} = \begin{cases} r_1 + p_1, n = 2k + 1 \\ 2p_1, n = 2(k + 1) \end{cases} (k = 1,2,3\ldots) \tag{26}$$

$$F_1 = min(F_{1a}, F_{1b}, F_{1c}, F_{1d}) \tag{27}$$

2.2. The multi-objective nonlinear optimization process of the optimizable parameters using the NSGA-II method

First, consider F_1 and F_2 as two separate objective values. Employ the NSGA-II algorithm to find the six optimizable parameters that maximize F_1 and F_2. These parameters can be expressed in vector form, as shown in Equation (28).

$$\vec{x} = [\alpha \quad r_1 \quad h \quad c \quad n \quad t]^T \tag{28}$$

Given the correlation between the two sub-objectives, F_1 and F_2, in this multi-objective optimization problem, improving one sub-objective tends to come at the expense of the other. Achieving simultaneous optimization of both objectives is not feasible. Multi-objective optimization aims to coordinate and balance between them, providing a set of solutions for users based on their requirements. The NSGA-II algorithm identifies the set of solutions as the Pareto front[11], where each element in this set represents a non-dominated optimal solution. The objective functions for F_1 and F_2 concerning each optimizable parameter are established using the mathematical model. Then, set the constraints for solving as shown in Equations (29) and (30), $\vec{x}_i$, $\vec{l}_{bi}$, $\vec{u}_{bi}$are elements in the $\vec{x}$, $\vec{l}_b$, $\vec{u}_b$ vectors, respectively, where *i* can be any integer between 1 and 6.

$$\vec{l}_{bi} \le \vec{x}_i \le \vec{u}_{bi}, i = 1,2,3\ \ldots \tag{29}$$

$$\begin{cases} \vec{l}_b = [0 \quad 1 \quad 2 \quad 0.05 \quad 3 \quad 0.004]^T \\ \vec{u}_b = [1.6 \quad 2 \quad 2.5 \quad 0.15 \quad 8 \quad 0.012]^T \end{cases} \tag{30}$$

DOI: 10.54254/2755-2721/86/20241600

Each optimizable parameter undergoes multiplication by a specific coefficient during optimization to unify their magnitudes, thereby facilitating the subsequent drawing of the 3D Pareto Front image [12]. Since the expressions for p_{1k} and p_{2k} differ when n is odd and even, two separate cases are solved. The population size is 50, with a crossover probability of 0.8, and the NSGA-II algorithm runs for 100 iterations. **Table 1** and **Table 2** display the solution sets, while **Figure 3** illustrates the solving process.

Table 1. The Optimization Results based on NSGA-II when n is odd

Serial Number	$\vec{x}$						$\vec{F}_{val}$	
	α (rad)	r_1 (m)	h (m)	$10 \cdot c$ (m)	n	$100 \cdot t$ (m)	F_1 (kN)	F_2 (kN)
1	0.9090	1.0856	2.1462	1.4982	6.9584	1.1894	142	52
2	1.5707	1.9795	2.0107	1.4987	6.9794	1.1760	10883	22
3	1.5670	1.9985	2.0078	1.4900	6.9612	1.1581	9159	22
4	1.5513	1.9985	2.0078	1.4990	6.9612	1.1581	2404	23
5	0.6478	1.0440	2.1545	1.4983	6.9690	1.1889	115	87
6	0.3822	1.6339	2.1757	1.4998	6.9830	1.1722	14	176
7	0.7679	1.0508	2.1829	1.4974	6.9418	1.1958	126	69
8	0.7015	1.0415	2.1567	1.4981	6.9370	1.1863	119	78
9	0.7939	1.0643	2.1501	1.4983	6.9648	1.1891	128	65
10	0.8489	1.0513	2.1475	1.4977	6.9428	1.1732	135	58
11	1.0354	1.1893	2.1508	1.4992	6.9502	1.1623	154	41
12	1.5686	1.9985	2.0077	1.4988	6.9742	1.1647	9848	22
13	1.5678	1.9985	2.0116	1.4991	6.9706	1.1594	9490	22
14	0.4241	1.6648	2.1791	1.4999	6.9962	1.1177	29	157
15	1.5697	1.9982	2.0096	1.4985	6.9858	1.1773	10423	22
16	0.4543	1.6030	2.1568	1.4996	6.9750	1.1724	49	143
17	0.7141	1.0477	2.1651	1.4978	6.9394	1.1929	120	76
18	0.4017	1.9735	2.1406	1.4991	6.9750	1.1720	25	167
19	1.5707	1.9795	2.0107	1.4987	6.9794	1.1760	10883	22
20	1.3810	1.6836	2.1674	1.4987	6.9824	1.1444	293	26
21	1.5425	1.9928	2.0070	1.4988	6.9702	1.1557	1662	23
22	0.5165	1.3038	2.1393	1.4985	6.9686	1.1969	80	119
23	0.4945	1.5091	2.1279	1.4993	6.9650	1.1802	70	127
24	1.5690	1.9983	2.0109	1.4985	6.9780	1.1738	10112	22
25	0.4980	1.3881	2.1241	1.4991	6.9622	1.1897	73	125
26	0.5930	1.1728	2.1778	1.4981	6.9794	1.1986	99	101
27	0.4705	1.6389	2.1161	1.4910	6.9750	1.1966	61	134
28	0.4125	1.9711	2.5000	1.5000	7.0000	1.2000	5	186
29	1.3042	2.0000	2.0000	1.5000	6.5736	1.2000	165	34
30	1.5616	2.0000	2.0000	1.5000	7.0000	1.2000	5291	23
31	1.3992	2.0000	2.0000	1.5000	7.0000	1.2000	286	30
32	1.5044	2.0000	2.0000	1.4928	7.0000	1.2000	724	25
33	0.4125	1.9711	2.5000	1.5000	7.0000	1.2000	5	186
34	1.4987	2.0000	2.0000	1.4990	7.0000	1.2000	675	25
35	1.5646	2.0000	2.0000	1.5000	7.0000	1.2000	7862	23
36	1.2823	2.0000	2.0000	1.4618	7.0000	1.2000	158	34
37	1.3944	2.0000	2.0000	1.5000	7.0000	1.2000	278	30

DOI: 10.54254/2755-2721/86/20241600

Table 1. (continued).

38	1.5139	2.0000	2.0000	1.5000	7.0000	1.2000	857	25
39	0.5672	1.0092	2.0000	1.5000	7.0000	1.2000	114	98
40	1.5346	2.0000	2.0000	1.5000	7.0000	1.2000	1348	24

Table 2. The Optimization Results based on NSGA-II when n is even

Serial Number	$\vec{x}$						$\vec{F}_{val}$	
	α (rad)	r_1 (m)	h (m)	$10 \cdot c$ (m)	n	$100 \cdot t$ (m)	F_1 (kN)	F_2 (kN)
1	0.3713	1.6739	2.3618	1.4935	7.8594	1.1868	12	203
2	1.5708	1.9705	2.3362	1.4947	7.8094	1.1909	12277	22
3	0.4352	1.6429	2.3521	1.4955	7.8440	1.1881	44	170
4	0.6592	1.2486	2.3226	1.4957	7.8828	1.1903	126	98
5	1.0120	1.0943	2.2029	1.4949	7.9008	1.1930	214	46
6	1.4287	1.9763	2.1405	1.4964	7.8394	1.1900	441	30
7	0.5854	1.1147	2.2668	1.4956	7.8886	1.1906	106	111
8	0.9345	1.0978	2.3694	1.4962	7.9086	1.1947	192	56
9	0.7378	1.1011	2.1700	1.4964	7.8994	1.1934	153	77
10	0.5361	1.5548	2.2229	1.4905	7.8644	1.1919	89	125
11	0.4084	1.6843	2.3193	1.4965	7.8554	1.1922	34	181
12	0.4303	1.7443	2.1901	1.4973	7.8420	1.1890	54	162
13	0.5544	1.1534	2.1916	1.4962	7.8728	1.1901	102	115
14	0.4978	1.9654	2.1958	1.4978	7.8404	1.1905	71	141
15	0.4440	1.7382	2.1544	1.4969	7.8510	1.1901	63	155
16	0.4887	1.6846	2.1239	1.4953	7.8220	1.1927	81	136
17	0.3872	1.7586	2.3551	1.4951	7.8474	1.1878	20	195
18	0.3886	1.6758	2.3475	1.4965	7.8572	1.1874	22	193
19	1.2558	1.6534	2.2659	1.4958	7.9146	1.1895	245	36
20	0.4926	1.4442	2.1471	1.4972	7.8498	1.1919	82	134
21	1.5700	1.9963	2.1644	1.4972	7.8372	1.1913	11941	23
22	0.6662	1.1017	2.1251	1.4977	7.8748	1.1998	145	88
23	0.3655	1.2840	2.5000	1.5000	8.0000	1.2000	4	218
24	1.5576	2.0000	2.0000	1.5000	8.0000	1.2000	4934	25
25	1.5036	2.0000	2.0000	1.5000	8.0000	1.2000	968	27
26	1.5368	2.0000	2.0000	1.5000	8.0000	1.2000	1908	26
27	1.5675	2.0000	2.0000	1.5000	8.0000	1.2000	11162	25
28	1.5217	2.0000	2.0000	1.5000	8.0000	1.2000	1323	27
29	1.5637	2.0000	2.0000	1.5000	8.0000	1.2000	9153	25
30	1.5439	2.0000	2.0000	1.5000	8.0000	1.2000	2414	26
31	1.5513	2.0000	2.0000	1.5000	8.0000	1.2000	3335	25
32	1.5698	1.0448	2.3915	1.4990	7.9870	1.1991	12689	9
33	1.5696	1.2304	2.0756	1.4999	7.9596	1.1980	12505	12

Based on the preceding analysis and the inherent characteristics of the NSGA-II algorithm, it is evident that the solutions presented in **Table 1** and **Table 2** represent optimal outcomes. Choosing the final solution requires considering the direction of the impact load that the resistance frame frequently

DOI: 10.54254/2755-2721/86/20241600

encounters. First, a rough analysis of the variations of F_1 and F_2 concerning each parameter is necessary to ensure the feasibility of transforming the multi-objective optimization problem into a single-objective optimization problem. Upon examining **Table 1**, **Table 2**, and **Figure 3**, it becomes evident that regardless of whether n is odd or even, among the six optimizable parameters, only α lacks a concentrated value. Hence, the hypothesis is that when aiming to optimize F_1 and F_2, α may not have a distinct optimization convergence direction. Ensuring that introducing the relationship between F_1 and F_2 in a multi-parameter scenario can lead to a unique solution in single-objective optimization requires verifying that at least one parameter can cause F_1 and F_2 to exhibit different variation trends and intersect. Since only α lacks an obvious concentration point in **Table 1**, and considering the mathematical model, it is not difficult to find that α appears in both the numerator and denominator of the expressions for F_1 and F_2, α is chosen as the parameter to be verified.

2.3. Analysis of the variation trends of F_1 and F_2 concerning α when n takes different values

As shown in **Figure 4**, when n takes different values, extract ten equally spaced α values in the range [0.6, 1.5] and the corresponding F_1 and F_2 values for each α. Establish a spatial Cartesian coordinate system with n as the x-axis, α as the y-axis, and F values as the z-axis, and plot the above sample points within the coordinate system. Construct the fitted curves of F_1 and F_2 concerning α for different n values based on these sample points, and observe the variation pattern of the intersection points between the fitted curves of F_1 and F_2 concerning α as n changes.

It is not difficult to see that, in the given range, as n gradually increases, the intersection points between the Polynomial Fit of F_1 curve and the Polynomial Fit of F_2 curve gradually approach the lower bound of the α domain, and both the Polynomial Fit of F_1 and Polynomial Fit of F_2 curves move upward along the z-axis. The pattern indicates that within the set range, regardless of the value of n, there will be an intersection point between the Polynomial Fit of the F_1 curve and the Polynomial Fit of the F_2 curve, which shows that F_1 tends to decrease with increasing α, and F_2 tends to increase with growing α. The pattern also implies that, with other conditions unchanged, a larger α improves the vertical impact resistance of the resistance frame, whereas a smaller α improves the horizontal impact resistance. Additionally, increasing n enhances the resistance frame's vertical and horizontal impact resistance because the newly added lateral edges share the high load previously borne by each lateral edge.

When all optimizable parameters exhibit a definite change trend, the GA solver can find a unique solution that meets the objective by incorporating additional constraints[13]. Finding the intersection points between the Polynomial Fit of F_1 and the Polynomial Fit of F_2 for different n values is equivalent to setting the optimization objective to find the optimizable parameters that make F_1 and F_2 equal. However, having F_1 and F_2 equal does not necessarily mean that the resistance frame has the optimal impact resistance. Therefore, it is necessary to discuss the value of the ratio n_q of F_1 to F_2 when the resistance frame achieves the optimal impact resistance[14]. Matrices (31) and (32) show the coefficient matrices for the Polynomial Fit of F_1 and F_2. Equation (33) gives the relationship between the coefficient matrix and the system of equations formed by the fitting curves. Here $\vec{v}$ is a multifaceted vector about α, and$\vec{s}_1$ and$\vec{s}_2$ are multidimensional vectors relating to F_1 and F_2. The forms of the vectors $\vec{v}$, $\vec{s}_1$, and $\vec{s}_2$ are shown in Equation (34).

$$B_1 = \begin{bmatrix} 5196187 & -25035682 & 47442348 & -44083619 & 20070008 & -3563979 \\ 8979404 & -43263370 & 81983085 & -76178195 & 34680974 & -6158207 \\ 10594917 & -51046870 & 96732197 & -89882291 & 40919300 & -7265456 \\ 15585147 & -75086040 & 142279355 & -132198825 & 60181791 & -10684882 \\ 19121092 & -92131068 & 174593527 & -162236068 & 73860524 & -13113904 \\ 25459177 & -122659604 & 232426089 & -215955966 & 98308929 & -17452984 \end{bmatrix} \quad (31)$$

DOI: 10.54254/2755-2721/86/20241600

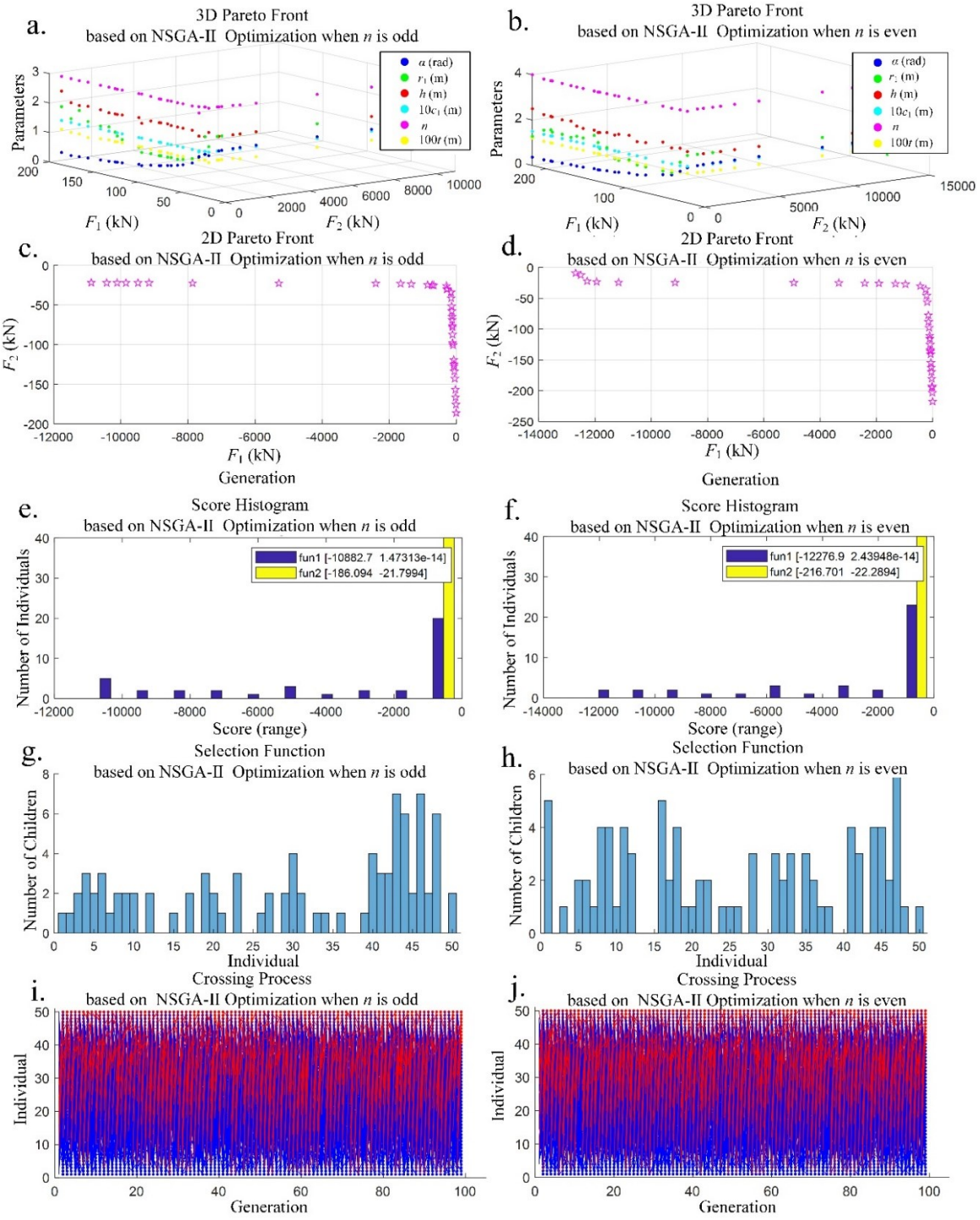

Figure 3. Pareto Front and the NSGA-II solving process. (Note: **a.** 3D Pareto Front based on NSGA-II Optimization when *n* is odd; **b.** 3D Pareto Front based on NSGA-II Optimization when *n* is even; **c.** 2D Pareto Front based on NSGA-II Optimization when *n* is odd; **d.** 2D Pareto Front based on NSGA-II Optimization when *n* is even; **e.** Score Histogram based on NSGA-II Optimization when *n* is odd; **f.** Score Histogram based on NSGA-II Optimization when *n* is even; **g.** Selection Function based on NSGA-II Optimization when *n* is odd; **h.** Selection Function based on NSGA-II Optimization when *n* is even; **i.** Crossing Process based on NSGA-II Optimization when *n* is odd; **j.** Crossing Process based on NSGA-II Optimization when *n* is even.)

DOI: 10.54254/2755-2721/86/20241600

$$B_2 = \begin{bmatrix} -52932 & 330754 & -842062 & 1114034 & -807533 & 284756 \\ -62300 & 390477 & -999685 & 1333405 & -987215 & 371969 \\ -65314 & 408875 & -1045290 & 1391300 & -1025207 & 382623 \\ -68834 & 430971 & -1102806 & 1470075 & -1087841 & 412430 \\ -70750 & 442721 & -1132031 & 1507416 & -1112423 & 418853 \\ -73146 & 457684 & -1170659 & 1559747 & -1152832 & 436849 \end{bmatrix} \tag{32}$$

$$\begin{cases} \vec{s}_1 = B_1\vec{v} \\ \vec{s}_2 = B_2\vec{v} \end{cases} \tag{33}$$

$$\begin{cases} \vec{s}_1 = [F_{1|n=3} \quad F_{1|n=4} \quad F_{1|n=5} \quad F_{1|n=6} \quad F_{1|n=7} \quad F_{1|n=8}]^T \\ \vec{s}_2 = [F_{2|n=3} \quad F_{2|n=4} \quad F_{2|n=5} \quad F_{2|n=6} \quad F_{2|n=7} \quad F_{2|n=8}]^T \\ \vec{v} = [\alpha^5 \quad \alpha^4 \quad \alpha^3 \quad \alpha^2 \quad \alpha^1 \quad \alpha^0]^T \end{cases} \tag{34}$$

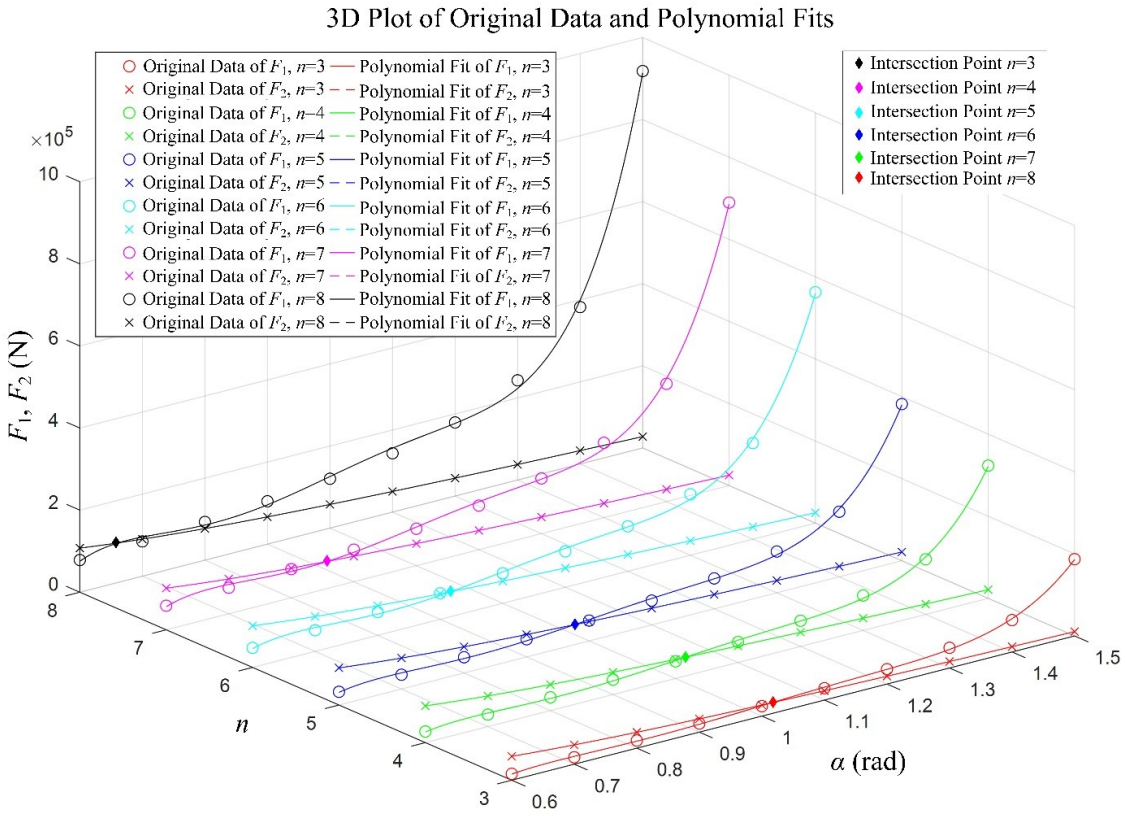

Figure 4. The relationship between the changes in F_1 and F_2 concerning α for different n.

2.4. Formatting author affiliations Determination of the Optimization Ratio and Objective Function for F_1 and F_2 in Single-Objective Optimization Using GA

Considering that the primary usage scenario for this resistance frame is residential buildings, it is preferable to determine the value of n_q based on this analysis background. Other usage scenarios, such as tunnels, mines, underground shelters, etc., would require specific analysis based on their respective environments. According to GB50096-2011, the commonly used floor height H is 2.8m. Since the most common impact load that the resistance frame needs to withstand comes from falling ceiling debris within buildings, the direction of the common impact load is normal to the contact surface when one side of the ceiling contacts the top surface of the resistance frame. To ensure the resistance frame has the best impact resistance under common loading conditions, Equation (35) shows a proportional relationship between F_1 and F_2. Here, d_w represents the shortest distance from the bottom edge of the resistance frame to the adjacent sidewall in space; in this case, d_w is set to 0.2m according to the

DOI: 10.54254/2755-2721/86/20241600

installation preset. Based on this proportional relationship, introduce $F_{1\zeta}$ as an intermediate variable related to F_1. The expression for $F_{1\zeta}$ is shown in Equation (36). To simultaneously optimize the resistance frame's vertical and horizontal impact resistance, a single-objective optimization objective function is set as Equation (37).

$$\frac{F_1}{F_2} = n_q = \frac{p_{2k}+d_w}{H-h} \tag{35}$$

$$F_{1\zeta} = \frac{F_1}{n_q} \tag{36}$$

$$F_{obj}(\alpha, r_1, h, c, n, t) = -(\sqrt{F_{1\zeta}^2 + F_2^2} - |F_{1\zeta} - F_2|) \tag{37}$$

2.5. The single-objective optimization process using GA

Given the same conditions, a GA solver was used to solve for x, with the maximum number of generations set to 500 and the stagnation limit set to 30. The initial points, value ranges[15], and optimal solutions are shown in **Table 3**, while the optimization process is illustrated in **Figure 5**. The iterative solver stops when the convergence criteria are met, yielding a unique optimal solution, as shown in **Table 3**. By comparing the parameters for n being odd and n being even, it can be seen that the optimal solution for h_{gq} is lower when n is even than when n is odd. A lower centre of gravity height indicates better frame stability. Thus, a frame with the optimal solution for n even possesses better lateral impact resistance. This can also be observed from the F_2 value derived by substituting the six optimizable parameters into the mathematical model mentioned earlier.

Moreover, the absolute value of F_{obj} is greater for n being even than for n being odd. According to the definition of the single-objective optimization function, the frame with the optimal solution for n being even has better overall impact resistance compared to the frame with the optimal solution for n being odd. The choice of n is odd or has little effect on the optimal solutions for the optimal angle β_b, the effective radius c of the profile cross-section, the frame height h, the effective radius r_1 of the top surface, and the wall thickness t of the profile. Based on the above analysis, the final global optimal solution is chosen from the optimal solutions for n being; even thus, when the optimizable parameters' vector $\vec{x} \approx [1.25 \quad 2 \quad 2 \quad 0.15 \quad 8 \quad 0.012]^T$ is used, the support frame can achieve the optimal impact resistance performance under the conditions specified in **Table 3**.

Substituting the optimal solution obtained from **Table 3** back into Equation (5), the effective radius at the bottom of the frame, r_2 is approximately 2.5 meters. This results in a maximum ground diameter, d_2, which can be roughly estimated as double that radius, yielding a value of approximately 5 meters. This ground area will limit the frame to being fixed in large open spaces within buildings, such as halls or auditoriums. This not only makes transportation and mobility inconvenient but also prevents the frame from being flexibly installed in relatively more minor spaces such as corridors and bedrooms, failing to meet the initial research objective of expanding the application scenarios of the impact-resistant frame.

Therefore, it is necessary to add a constraint to the single-objective optimization. Based on the characteristics of internal spaces in residential buildings and construction standards, the maximum ground diameter of the frame is limited to no more than 3.4m, i.e., the effective radius at the bottom of the frame is limited to no more than 1.7m. Considering this constraint and engineering factors such as welding processes, the optimization parameter range was redefined, and the GA method was used again for single-objective optimization of the frame. The objective function and other preset conditions remain the same as those used in the previous single-objective optimization process. The new optimization results are shown in **Table 4**.

DOI: 10.54254/2755-2721/86/20241600

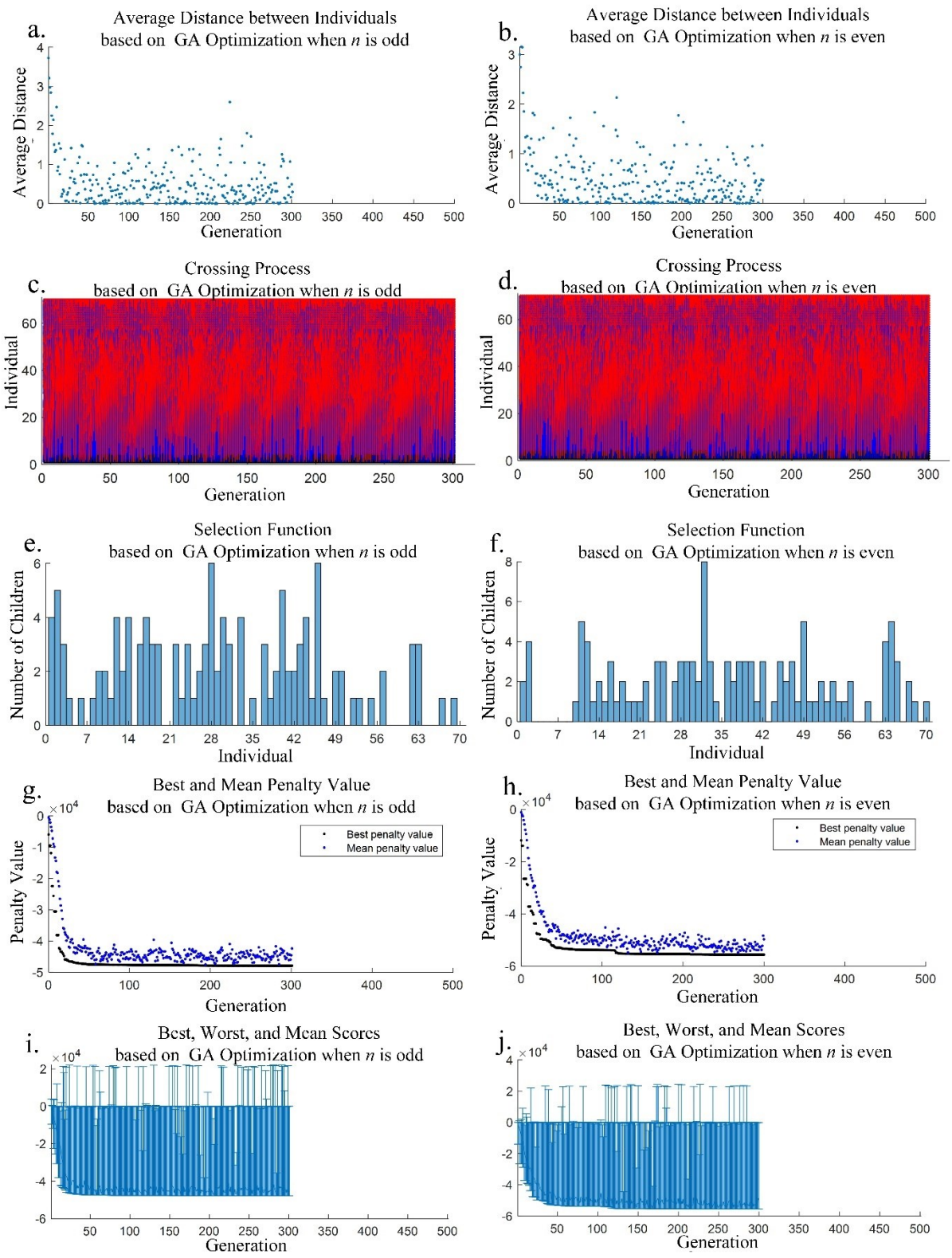

Figure 5. The process of single-objective nonlinear optimization uses the GA solver with no additional constraints.

DOI: 10.54254/2755-2721/86/20241600

(Note: **a.** Average Distance between Individuals based on GA Optimization when n is odd; **b.** Average Distance between Individuals based on GA Optimization when n is even; **c.** Crossing Process based on GA Optimization when n is odd; **d.** Crossing Process based on GA Optimization when n is even; **e.** Selection Function based on GA Optimization when n is odd; **f.** Selection Function based on GA Optimization when n is even; **g.** Best and Mean Penalty Value based on GA Optimization when n is odd; **h.** Best and Mean Penalty Value based on GA Optimization when n is even; **i.** Best, Worst, and Mean Scores based on GA Optimization when n is odd; **j.** Best, Worst, and Mean Scores based on GA Optimization when n is even.)

Similarly, within the new parameter range, the optimal values of F_1, F_2, and F_{obj} for n are even higher than those for n is odd. Therefore, the optimal solution for n=8 is chosen as the new optimal parameter for the frame, which provides the best impact resistance performance within the given parameter range.

Table 3. The results of the single-objective nonlinear optimization using the GA solver under no additional constraints.

Parameters	Value when n is odd			Value when n is even		
	Range	Initial	Optimal	Range	Initial	Optimal
α (rad)	0.0000~1.6000	0.8000	1.3155	0.0000~1.6000	0.8000	1.2553
r_1 (m)	1.0000~2.0000	1.7500	1.9800	1.0000~2.0000	1.7500	1.9370
h (m)	2.0000~2.5000	2.2500	2.0284	2.0000~2.5000	2.2500	2.0023
c (m)	0.1500~0.2000	0.1750	0.1500	0.1500~0.2000	0.1750	0.1500
n	3.0000~7.0000	5.0000	7.0000	4.0000~8.0000	6.0000	8.0000
t (m)	0.0080~0.0120	0.0100	0.0120	0.0080~0.0120	0.0100	0.0120
h_{gq} (m)	–	–	0.9093	–	–	0.8809
β (rad)	–	–	1.3910	–	–	1.3908
n_q	–	–	5.8299	–	–	5.4944
F_1 (N)	–	–	20.5700×10^4	–	–	21.6163×10^4
F_2 (N)	–	–	3.5529×10^4	–	–	3.9348×10^4
F_{obj} (N)	–	–	-4.9716×10^4	–	–	-5.5637×10^4

Table 4. The single-objective nonlinear optimization results using the GA solver under additional constraints.

Parameters	Value when n is odd			Value when n is even		
	Range	Start	Optimal	Range	Start	Optimal
α (rad)	0.0000~1.6000	0.8000	1.2795	0.0000~1.6000	0.8000	1.2403
r_1 (m)	1.0000~1.5000	1.2500	1.0001	1.0000~1.5000	1.2500	1.0107
h (m)	2.0000~2.3000	2.1500	2.0039	2.0000~2.3000	2.1500	2.0124
c (m)	0.0800~0.1800	0.1300	0.1800	0.0800~0.1800	0.1300	0.1800
n	3.0000~7.0000	5.0000	7.0000	4.0000~8.0000	6.0000	8.0000
t (m)	0.0080~0.0120	0.0100	0.0120	0.0080~0.0120	0.0100	0.0118
h_{gq} (m)	–	–	0.7925	–	–	0.7849
β_b(rad)	–	–	1.2675	–	–	1.2875
n_q	–	–	5.6059	–	–	3.3521
F_1 (N)	–	–	62.7640×10^4	–	–	68.3208×10^4
F_2 (N)	–	–	3.2350×10^4	–	–	3.7213×10^4
F_{obj} (N)	–	–	-3.4996×10^4	–	–	-4.0663×10^4

DOI: 10.54254/2755-2721/86/20241600

3. Finite Element Simulation Experiment

To better align with engineering practice, the optimal parameters obtained for even values of n in **Table 4** are approximated, i.e., based on $\vec{x}_b \approx [1.25 \quad 1 \quad 2 \quad 0.18 \quad 8 \quad 0.012]^T$. The frame designed with these parameters can meet more internal layout conditions of buildings while possessing the best overall impact resistance performance. To verify the correctness of the optimization results, a three-dimensional model of the resisting frame was built using $\vec{x}_b$ as the design parameters for the experimental group. The control group was a resisting frame appropriately modified from a rectangular configuration. Material properties were substituted, and a rectangular falling block with a 15° angle to the horizontal direction (impact angle $\beta = 75°$) was selected as the impact load source[16]. The height of the centroid of the falling block is equal to H, and the gravity g is 9.8 m/s². The impact test simulation results are shown in **Figure 6**.

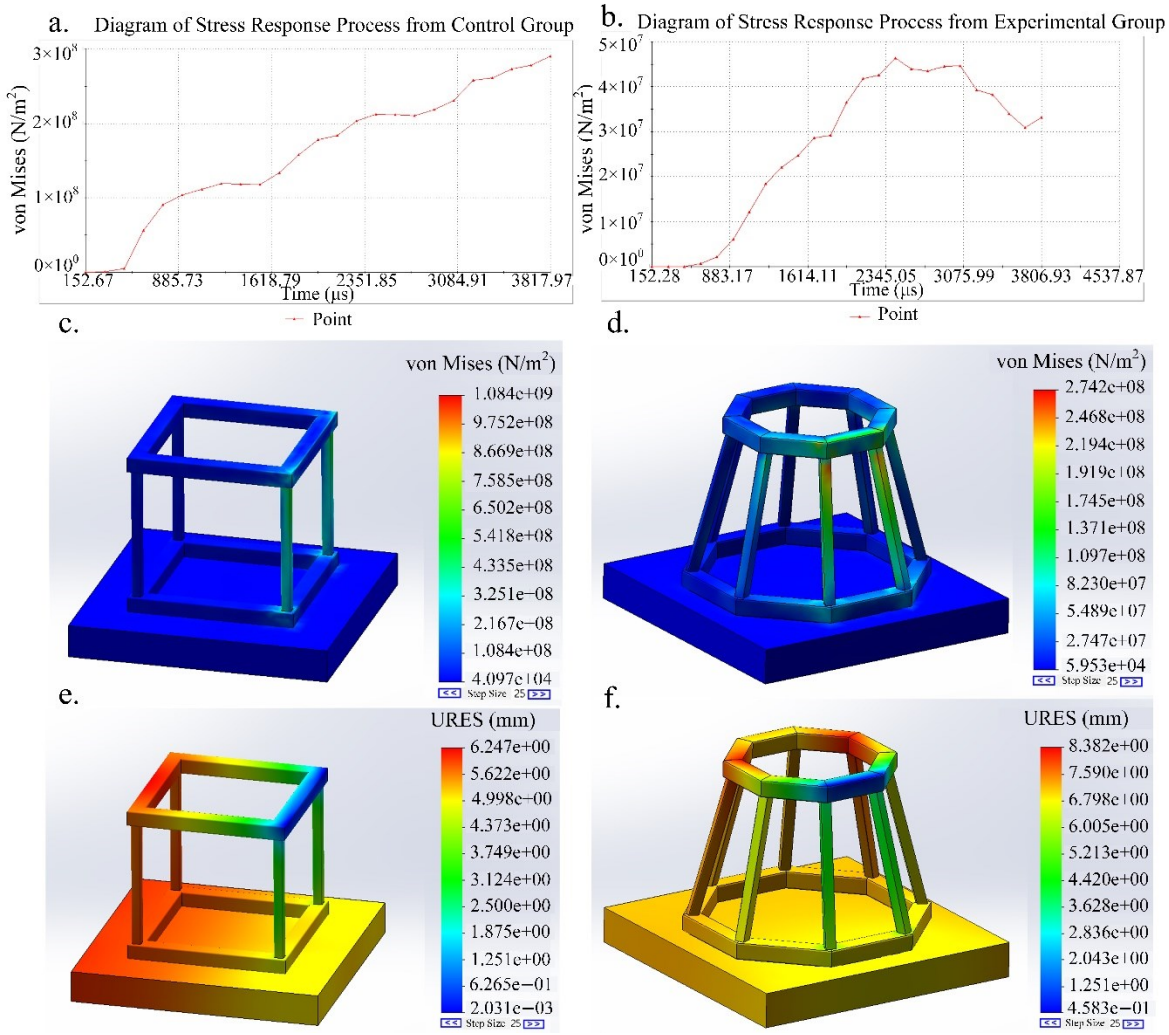

DOI: 10.54254/2755-2721/86/20241600

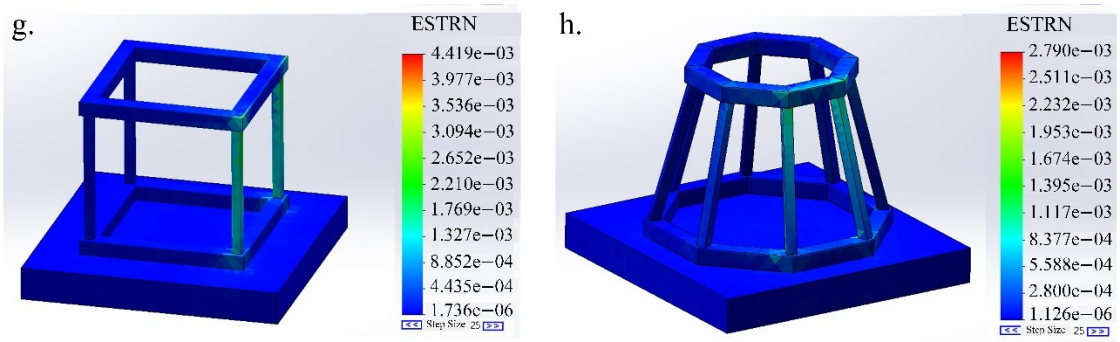

Figure 6. Finite element impact results of the optimized resistance frame compared with those of the traditional resistance frame. (Note: **a.** Diagram of Stress Response Process from Control Group; **b.** Diagram of Stress Response Process from Experimental Group; **c.** Control group's von Mises stress contour plot; **d.** Experimental group's von Mises stress contour plot; **e.** Control group's displacement contour plot; **f.** Experimental group's displacement contour plot; **g.** Comparison group's strain contour plot; **h.** Experimental group's strain contour plot.)

It can be observed that during the impact process, the maximum values of stress, displacement, and strain in the experimental group frame are all lower than those in the control group frame. The experimental group exhibits a specific rebound characteristic within the same impact duration. In contrast, the control group does not, indicating that the toughness of the experimental group frame is higher than that of the control group. As mentioned above, the simulation further confirms that the optimal impact-resistant frame for different layout scenarios can be obtained through this method. The resulting frame possesses better overall impact resistance than frames based on general geometric configurations such as rectangular shapes.

4. Conclusion

This method can obtain the unique optimal solution for six optimizable parameters under different layout conditions. The frame constructed based on this unique optimal solution possesses the best overall impact resistance performance under the given layout conditions.

4.1. Conclusions regarding the six optimizable parameters

When other parameters remain constant, the value of r_1 is related to the rate of change and intersection positions of the Polynomial Fit of F_1 and Polynomial Fit of F_2 in **Figure 4**, the range of r_1, and whether additional constraints regarding the frame's footprint are applied. Without additional footprint constraints, increasing r_1 enhances the frame's horizontal impact resistance while vertical impact resistance remains unchanged, thereby improving overall impact resistance. However, with additional footprint constraints, the single-objective optimization function relates to F_1 and F_2. Thus, r_1 may tend towards its range's lower or upper bounds, depending on its effect on the rates of change in F_1 and F_2 and the intersection positions of the Polynomial Fit of F_1 and Polynomial Fit of F_2 in **Figure 4**. The h trend also depends on its range, the layout conditions (such as H, d_w, etc.), and additional footprint constraints. There is no fixed trend.

For c, n, and t, when other parameters remain constant, increasing these three parameters improves the impact resistance of the frame. This is because increasing c, n, and t increases the effective cross-sectional area of the profile to varying degrees, distributing the original cross-sectional stress and allowing the frame to withstand higher lateral and vertical impact loads.

When n is even, the frame's overall impact resistance is better when n takes the most significant even number within its range than when it takes the most significant odd number. This is also due to increased permissible load from the improved effective cross-sectional area. However, whether the economic marginal benefit of increasing n by 1 is significant requires further analysis.

DOI: 10.54254/2755-2721/86/20241600

Additionally, for n, a reasonable hypothesis is that as $n \to \infty$, i.e., when the frustum cone becomes a cylinder (ignoring cost and structural topology details), the frame will have better overall impact resistance.

The optimal solution for α is related to n_q, which is in turn related to h. Thus, α is influenced by multiple factors. When other parameters remain constant, a larger α improves vertical impact resistance, while a smaller α enhances horizontal impact resistance. The specific optimal solution for α is determined by the comprehensive factors of the frame's layout scenario.

4.2. Conclusions regarding geometric configuration

A right frustum frame has better overall impact resistance than a rectangular frame. This is primarily because the centre of gravity of a right frustum frame is generally lower than that of a rectangular frame of the same height, providing better horizontal impact resistance. Additionally, a right frustum frame has better symmetry than a rectangular or general frustum frame, thus exhibiting better impact resistance from various directions.

4.3. Other conclusions

The unique optimal solution of the frame is based on the specific layout scenario and corresponds to impact loads in a particular direction for that scenario. The optimal impact resistance angle for the optimal frame in each layout scenario is a specific value at which the frame can achieve the optimal F_{obj} value, i.e., the maximum F_{obj} within a given range. Therefore, when facing impacts from other angles, the optimal frame still possesses locally optimal impact resistance compared to other frames.

References

[1] Bolt, B.A., et al., *Geological Hazards: Earthquakes-tsunamis-volcanoes-avalanches-landslides-floods.* 2013: Springer Science & Business Media.

[2] Holzer, T.L. and J.C. Savage, *Global earthquake fatalities and population.* Earthquake Spectra, 2013. 29(1): p. 155-175.

[3] Popov, E.P., C.E. Grigorian, and T.-S. Yang, *Developments in seismic structural analysis and design.* Engineering structures, 1995. 17(3): p. 187-197.

[4] Ferreira, J.G., et al., *SHELTER–Structural Hyper-resisting Element for Life Threatening Earthquake Risk. An innovative approach for seismic protection*. Engineering Structures, 2021. 235: p. 112012.

[5] Hosseini, S., et al., *SHELTER–Structural Hyper-resisting element for life Threatening Earthquake Risk. Static tests on the shelter structure.* Journal of Building Engineering, 2022. 47: p. 103824.

[6] Ma, H., et al., *A comprehensive survey on NSGA-II for multi-objective optimization and applications.* Artificial Intelligence Review, 2023. 56(12): p. 15217-15270.

[7] Hartshorne, R., *Geometry: Euclid and beyond*. 2013: Springer Science & Business Media.

[8] Meriam, J.L., L.G. Kraige, and J.N. Bolton, *Engineering mechanics: dynamics*. 2020: John Wiley & Sons.

[9] Krane, K.S., *Modern physics*. 2019: John Wiley & Sons.

[10] Craig Jr, R.R. and E.M. Taleff, *Mechanics of materials*. 2020: John Wiley & Sons.

[11] Deb, K., et al., *A fast and elitist multi-objective genetic algorithm: NSGA-II.* IEEE transactions on evolutionary computation, 2002. 6(2): p. 182-197.

[12] Verma, S., M. Pant, and V. Snasel, *A comprehensive review on NSGA-II for multi-objective combinatorial optimization problems*. IEEE access, 2021. 9: p. 57757-57791.

[13] Lambora, A., K. Gupta, and K. Chopra. *Genetic algorithm-A literature review. in 2019 international conference on machine learning, big data, cloud and parallel computing (COMITCon).* 2019. IEEE.

[14] Seber, G.A. and A.J. Lee, *Linear regression analysis*. 2012: John Wiley & Sons.

DOI: 10.54254/2755-2721/86/20241600

[15] Coello, C.A., *An updated survey of GA-based multi-objective optimization techniques.* ACM Computing Surveys (CSUR), 2000. 32(2): p. 109-143.
[16] Yarin, A.L., *Drop impact dynamics: Splashing, spreading, receding, bouncing….* Annu. Rev. Fluid Mech., 2006. 38: p. 159-192.